



# Strong circular dichroism in chiral plasmonic metasurfaces optimized by micro-genetic algorithm

ZHIGANG LI,<sup>1</sup> DANIEL ROSENMANN,<sup>2</sup> DAVID A. CZAPLEWSKI,<sup>2</sup>  
XIAODONG YANG,<sup>1,3</sup> AND JIE GAO<sup>1,4</sup>

<sup>1</sup>*Department of Mechanical and Aerospace Engineering, Missouri University of Science and Technology, Rolla, MO 65409, USA*

<sup>2</sup>*Center for Nanoscale Materials, Argonne National Laboratory, Argonne, IL 60439, USA*

<sup>3</sup>*yangxia@mst.edu*

<sup>4</sup>*gaojie@mst.edu*

**Abstract:** Strong circular dichroism in absorption in the near-infrared wavelength range is realized by designing binary-pattern chiral plasmonic metasurfaces via the micro-genetic algorithm optimization method. The influence of geometric parameter modifications in the binary-pattern nanostructures on the circular dichroism performance is studied. The strong circular dichroism in absorption is attributed to the simultaneous excitation and field interference of the resonant modes with relative phase delay under linearly polarized incident light. This work provides a universal design method toward the on-demand properties of chiral metasurfaces, which paves the way for future applications in chemical and biological sensing, chiral imaging and spectroscopy.

© 2019 Optical Society of America under the terms of the [OSA Open Access Publishing Agreement](#)

## 1. Introduction

Chiral structures are well known for lacking any mirror symmetry. Unlike chiral molecules or materials in nature with weak chirality, artificially designed chiral metamaterials, for instance, two-dimensional (2D) anisotropic chiral metamaterials [1–4], dual-layer or multilayer twisted structures [5–9], helical meta-atoms [10,11] and even achiral planar metasurfaces [12,13] can achieve giant chiral properties including optical rotation, circular dichroism and asymmetric transmission. Optical chirality has attracted great interest in chemical and biological sensing [7], high-contrast chiral imaging for display technology [14], and electro-optical signal manipulation [3]. Generally, 2D planar metasurfaces with strong chirality are more appealing for applications requiring compact device configuration and simple fabrication processes. However, there are two limitations to consider in metamaterials design: complexity and efficiency. Traditional design methods, depending mainly on manual parameter sweeping, involve only a few design variables and geometries with limited complexity in which the optimal solution could be missed. In terms of efficiency, manually conducted metamaterial design is usually intended for the specific design application, which is not efficient to serve as a universal design method.

The above-mentioned limitations can be overcome by utilizing optimization methods, such as evolutionary method [15–17], gradient descent method [18,19], particle swarm optimization [20,21], and learning method based on neural networks [22–25]. Among various optimization methods, the genetic algorithm, a popular branch of the evolutionary method due to its simple frame, flexibility and compatibility, has successfully demonstrated the robustness and efficiency in the optimization of the electromagnetic design, for applications including broadband light absorption under linear polarization [16,17,26,27], selective transmission under circular polarization [28,29], and broadband circular polarizer [30]. However, the mechanism of generating the strong circular dichroism with complex binary-pattern structures has not been thoroughly

studied yet. Moreover, compared to traditional genetic algorithm, micro-genetic algorithm is more viable for real applications since it increases the diversity of population and accelerates the evolution progress by replacing the mutation step in traditional genetic algorithm with the repopulation step by introducing new population with random chromosomes, and consequently requires smaller initial population group while offering faster convergence [31,32].

In this work, we employ the micro-genetic algorithm to optimize the design of binary-pattern chiral plasmonic metasurfaces for achieving strong circular dichroism in absorption (CDA), with distinct absorption values for left- and right-handed circularly polarized (LCP and RCP) light. Two types of binary-pattern nanostructures are obtained with strong CDA at the infrared wavelength of 1.62  $\mu\text{m}$  and 1.91  $\mu\text{m}$ , respectively. The influence of geometric parameter modifications on the circular dichroism is studied by involving single-pixel changes in the binary-pattern nanostructures. It is found that the strong CDA is achieved as a result of the simultaneous excitation and field interference of the resonant modes with relative phase delay under linearly polarized incident light. The energy dissipation inside the metasurfaces is also discussed. The proposed design method offers great potential to realize on-demand chiral metasurfaces with high performance, which are very attractive for applications in chemical and biological sensing, chiral imaging and spectroscopy.

## 2. Formulation of structural design with micro-genetic algorithm

According to the principle of micro-genetic algorithm, the optimization of chiral plasmonic metasurfaces is initialized with a random geometry for the binary-pattern nanostructure. The geometric information of the nanostructure is encoded into the chromosome, which is composed of binary numbers. In the discretized binary space, the binary numbers, one and zero, represent the material and free space, respectively. The binary-pattern nanostructure evolves toward the optimal geometry along the direction driven by the cost function, which evaluates the discrepancy between the CDA value for each generated nanostructure and the predefined target value. Let the cost function cast as  $F = \sum_{\lambda} (1 - |A_{LCP} - A_{RCP}|)^2$ , where  $A_{LCP}$  and  $A_{RCP}$  are the absorption of the nanostructure under the LCP and RCP incidence, respectively,  $\lambda$  denotes the wavelength in the target wavelength range. Thus,  $CDA = A_{LCP} - A_{RCP}$ . The evolutionary optimization problem can be mathematically written as: minimize  $F$ , subject to  $\nabla \times \nabla \times \mathbf{E} - \mu\omega^2 \epsilon \mathbf{E} = 0$  and  $\nabla \cdot \epsilon \mathbf{E} = 0$ , where  $\mathbf{E}$  denotes the electric field,  $\epsilon$  the permittivity and  $\mu$  the permeability. The formulated problem is then solved through the finite element method (commercial software, COMSOL). The calculation is implemented with periodic boundary condition and perfect matched layers, as well as adaptive mesh method with mesh grids fine enough to guarantee the accuracy. The cost value  $F$  is derived from the absorption spectra for each generated nanostructure. Based on the cost value  $F$ , the evolution loop will choose to update the chromosome information for a new calculation or stop the loop until the predefined target is satisfied in the program.

In this work, the target performance is expected to present strong chirality with the CDA over 0.5 for the designed binary-pattern metasurface under LCP and RCP incidence within a certain narrow wavelength range. We select 10 equally spaced test wavelengths in the wavelength range between 1.5  $\mu\text{m}$  to 1.75  $\mu\text{m}$  (or between 1.75  $\mu\text{m}$  to 2  $\mu\text{m}$ ) for the calculation. To increase the anisotropic properties and further reduce the complexity in the calculations, the binary-pattern metasurface employs a non-square 15 $\times$ 11 array with two-fold rotational symmetry and intentionally defined gap space between four quadrants. The evolutionary optimization is implemented by the micro-genetic algorithm with a population of 20 chromosomes and the tournament selection for crossover for each generation. When achieving the valve value of the similarity among chromosomes, the algorithm takes the repopulation step to increase diversity and speed up the evolution without the need of a mutation step. Eventually, with the convergence within 35 generations, this work finds two types of binary-pattern chiral plasmonic metasurfaces with high CDA values satisfying the predefined targets.

### 3. Design of binary-pattern chiral plasmonic metasurfaces

Metal-dielectric-metal three-layer films have been widely used for the metamaterial absorber designs [16,17,27], where large light absorption can be realized with the carefully designed nanostructures on the top metallic layer. In this work metal-dielectric-metal three-layer film is also used for achieving strong circular dichroism in absorption. The advantage of the flexible design capability in the top metallic layer can be further enhanced by implementing the optimal geometry generated in the micro-genetic optimization algorithm. Figure 1(a) presents the schematic of the designed binary-pattern chiral plasmonic metasurface with strong CDA. The designed metasurface consists of a 55 nm-thick top gold (Au) layer with Pattern A obtained from the optimization algorithm, a 145 nm-thick silica ( $\text{SiO}_2$ ) spacer layer and a 200 nm-thick Au substrate. As the substrate is optically thick enough to eliminate the transmission through the designed nanostructure, the absorption is calculated as unity minus the reflection upon the LCP or RCP incidence. Figure 1(b) shows the top view of the designed chiral metasurface with pattern A having a  $15 \times 11$  array composed of square gold pixels with sides of  $w = 64$  nm. The supercell pattern A contains two kinds of components with two-fold symmetry. Additionally, the material parameters in the simulation are taken from the references for Au [33] and  $\text{SiO}_2$  [34], respectively.

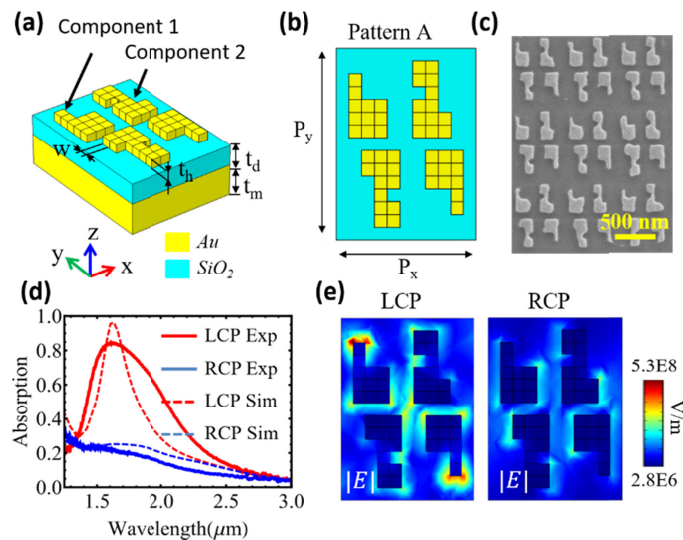


**Fig. 1.** (a) Schematic of the designed binary-pattern chiral plasmonic metasurface with pattern A. The geometric parameters are denoted as  $w = 64$  nm,  $t_h = 55$  nm,  $t_d = 145$  nm and  $t_m = 200$  nm. (b) Top view of the designed pattern A with period  $P_x = 704$  nm and  $P_y = 960$  nm. (c) SEM image of the fabricated chiral metasurface with pattern A. (d) Experimental (Exp) and simulated (Sim) absorption spectra under LCP and RCP incidence at normal direction, respectively. (e) Normalized electric field  $|E|$  distributions at the resonant wavelength of  $1.62 \mu\text{m}$  under LCP and RCP incidence, respectively, plotted at the surface of the top Au pattern.

The Au- $\text{SiO}_2$ -Au three-layer film is deposited on a glass substrate, with the Au layers deposited by using an electron-beam evaporator (Lesker PVD250) and the  $\text{SiO}_2$  layer deposited by reactive sputtering (Lesker CMS18). Next, the designed nanostructure array is milled in the top Au layer using a focused ion beam (FIB) system (FEI Helios Nanolab 600, 30 kV, 9.7 pA). Figure 1(c) shows a scanning electron microscopy (SEM) image of the fabricated chiral metasurface with pattern A, in which slight variations in the geometric parameters can be observed compared to the

designed nanostructure. The geometric variations are attributed to the fabrication imperfections, and the influences of those variations on circular dichroism will be discussed in the later Section. The fabricated chiral metasurface is then characterized with the Fourier transform infrared spectroscopy system (FTIR, Nicolet 6700). It is noted that the fabricated pattern array has an area of  $38 \mu\text{m}$  by  $28 \mu\text{m}$  while the spot size illuminated on the sample is around  $30 \mu\text{m}$  by  $20 \mu\text{m}$  to avoid the boundary influence in the FTIR measurement.

Figure 1(d) shows the measured and simulated absorption spectra ( $A_{LCP}$ ,  $A_{RCP}$ ) of the chiral metasurface under LCP and RCP incidence at the normal direction, respectively. The simulated absorption spectra of chiral metasurface with pattern A present strong circular dichroism, with a near perfect absorption of 0.96 under LCP incidence at the resonant wavelength of  $1.62 \mu\text{m}$  and a low absorption of 0.25 under RCP incidence. The chiral metasurface with pattern A then exhibits a high CDA value of 0.71 at  $1.62 \mu\text{m}$  in simulation, compared to the experimental value of 0.63. The discrepancy between the predicted and the experimental values arises mainly from the geometric variations produced during the fabrication. Figure 1(e) depicts the localization of the electric field  $|E|$  distribution and the high contrast of the electric field intensity between LCP and RCP excitations at the wavelength of  $1.62 \mu\text{m}$ . Giant CDA is induced by the dichroic resonant modes excited in the nanostructure under circularly polarized light.

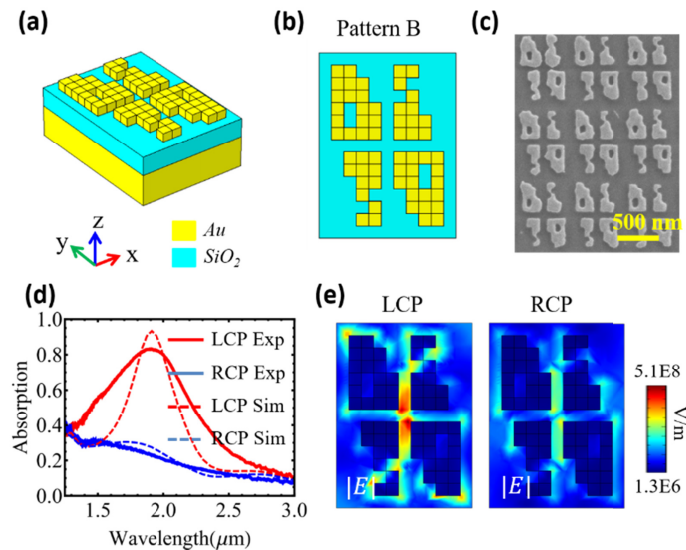


**Fig. 2.** (a) Schematic of the alternative designed binary-pattern chiral plasmonic metasurface with pattern B. (b) Top view of the designed pattern B. (c) SEM image of the fabricated chiral metasurface with pattern B. (d) Experimental (Exp) and simulated (Sim) absorption spectra under LCP and RCP incidence at normal direction, respectively. (e) Normalized electric field  $|E|$  distributions at the resonant wavelength of  $1.91 \mu\text{m}$  under LCP and RCP incidence, respectively, plotted at the surface of the top Au pattern.

By taking advantage of the flexibility in the micro-genetic algorithm optimization method, another example of chiral metasurface design with a different operating wavelength range is demonstrated by simply adjusting the condition setting in the predefined target and cost function. The same  $15 \times 11$  array of gold square pixels and material properties are employed in the optimization process in pattern B but with the target of achieving a CDA value over 0.5 in a different wavelength range of  $1.75 \mu\text{m}$  to  $2 \mu\text{m}$ . Figures 2(a) and 2(b) show the optimized chiral metasurface with pattern B. The supercell pattern B is also composed of two kinds of components with two-fold symmetry. A SEM image of the fabricated chiral metasurface with pattern B is

shown in Fig. 2(c). Figure 2(d) presents the measured and simulated absorption spectra under LCP and RCP incidence, respectively, showing the strong chirality. For LCP incidence, the chiral metasurface generates a strong absorption around 0.94 at the resonant wavelength of 1.91  $\mu\text{m}$ , leading to the simulated and measured CDA values of 0.67 and 0.60, respectively. As shown in Fig. 2(e), strong circular dichroic resonant modes are excited between the gaps of the four components in pattern B under LCP incidence, however, these modes are suppressed under RCP incidence.

#### 4. Influence of geometric parameter modifications on circular dichroism

The influence on circular dichroism performance caused by geometric parameter modifications in the binary-pattern nanostructures is studied in simulation to investigate the robustness and sensitivity of the circular dichroism in the optical response to geometric variations introduced during the fabrication process. By taking the chiral metasurface with pattern A as the example, in Figs. 3(a) and 3(b), we simulate the influence of increasing and decreasing the gap space by one-pixel distance along the  $x$  direction by shifting the two right components shown in the blue dashed box (pattern A1 and pattern A2), respectively. As shown in Fig. 3(d), the resonant wavelength in the absorption spectrum exhibits a redshift from 1.62  $\mu\text{m}$  to 1.67  $\mu\text{m}$  with almost perfect absorption under LCP incidence and a similar CDA of 0.74 for the chiral metasurface with pattern A1. In contrast, Fig. 3(e) shows a slight blueshift for the resonant wavelength to 1.61  $\mu\text{m}$  with the absorption of 0.9 under LCP incidence but a lower CDA of 0.62 for pattern A2 due to

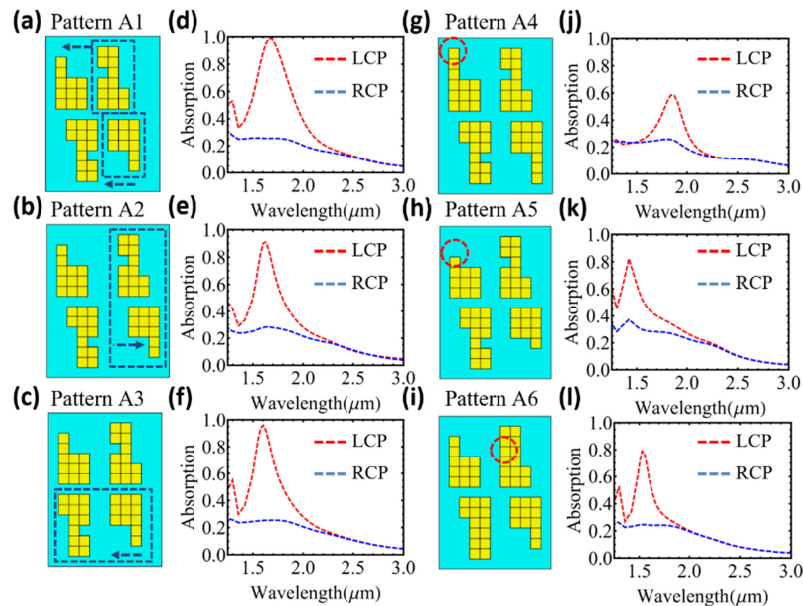


**Fig. 3.** The influence of geometric parameter modifications in the designed binary-pattern nanostructures on the circular dichroism performance. Schematics of (a) decreasing and (b) increasing the gap space along the  $x$  direction by shifting the two right components, and (c) geometric alignment by shifting the two bottom components shown in the blue dashed box to form pattern A1, pattern A2 and pattern A3, and (d)–(f) the corresponding simulated absorption spectra under LCP and RCP incidence. (g)–(i) Schematics of adding or removing pixels in supercell components shown in red dashed circle to form pattern A4, pattern A5 and pattern A6, and (j)–(l) the corresponding simulated absorption spectra under LCP and RCP incidence.

the reduced confinement of the resonant modes with the increased gap space. Moreover, Fig. 3(c) depicts the geometry alignment by shifting the two bottom components shown in the blue dashed box by one-pixel distance to the left along the  $x$  direction (pattern A3). Results of this alignment operation are plotted in Fig. 3(f) showing a resonance blueshift to  $1.60\ \mu\text{m}$  with the absorption of 0.95 and the almost unchanged CDA of 0.70 for pattern A3, which indicates the modification of mode coupling between the supercell components is almost negligible. Furthermore, geometric features of the supercell components in the designed chiral metasurfaces pattern A are modified by adding or removing pixels and thus three different cases are obtained. In Fig. 3(g), one pixel (in the red dashed circle) is added to Component 1 to extend its length (pattern A4), leading to an obvious resonance redshift from  $1.62\ \mu\text{m}$  to  $1.86\ \mu\text{m}$  with a much lower CDA of 0.34 as shown in Fig. 3(j). The degradation in the chirality performance is attributed to the weaker mode excitation of Component 1 due to the added pixel. In comparison, when one pixel is removed from Component 1 to shorten its length (pattern A5) as shown in Fig. 3(h), the resonance blueshift to  $1.42\ \mu\text{m}$  is observed with a low CDA of 0.45 as plotted in Fig. 3(k). Similarly, in Fig. 3(i), as one pixel (in the red dashed circle) is added in Component 2, the resonance is shifted to  $1.54\ \mu\text{m}$  with a low CDA of 0.55 as plotted in Fig. 3(l). Consequently, geometric parameter modifications introduced by adding or removing important pixel features will significantly degrade the circular dichroism performance for the designed chiral metasurfaces. The influence of critical pixel modification on CDA shows predominant influence compared to that produced by the shift or alignment of the supercell components. The influences of geometric variations studied here well explain the observed broadened resonant absorption peaks and circular dichroism values in experiment shown in Fig. 1(d) and Fig. 2(d).

## 5. Circular dichroic mode analysis

In order to elucidate the underlying mechanism behind the strong circular dichroism obtained in this work, we conduct further analysis of the circular dichroic mode distributions inside the designed chiral metasurface. For the chiral metasurface with pattern A, Fig. 4(b) plots the absorption spectra under  $x$ - and  $y$ - polarized light at normal incidence. Two resonant modes are observed, and the electric field  $E_x$  distributions at the wavelength of  $1.62\ \mu\text{m}$  for  $x$ -polarized (with phase of  $-90^\circ$  or  $90^\circ$ ) and  $y$ -polarized incidence (with phase of  $0^\circ$ ) are presented in Fig. 4(c) respectively. It is observed that there are two antiparallel dipole modes formed on each supercell component within pattern A. Moreover, when the chiral metasurface is excited with circularly polarized light, the corresponding dipole modes under  $x$ - and  $y$ -polarized incidence are simultaneously excited with relative phase delay of  $90^\circ$  or  $-90^\circ$ , leading to constructive or destructive field interferences to form the LCP or RCP resonant mode, respectively, as highlighted in two typical locations marked by red dashed circles and blue dashed boxes. Thus, the electric field is greatly enhanced under LCP excitation but significantly suppressed under RCP excitation with the  $E_x$  amplitude in the LCP mode around 5.6 times larger than that of the RCP mode, resulting in the observed strong circular dichroism.

With the purpose of understanding the degradation of chirality performance, circular dichroic mode analysis is also conducted for the chiral metasurface pattern A4 as an example. Unlike pattern A, pattern A4 shows the degraded CDA due to the geometric parameter variation in extending the length of Component 1 by adding one pixel. Figure 5(b) plots the absorption spectra of pattern A4 under  $x$ - and  $y$ - polarized incidence, exhibiting a lower absorption at the resonant wavelength of  $1.83\ \mu\text{m}$  and  $1.80\ \mu\text{m}$ , respectively. Also, the absorption peak for  $x$ -polarized incidence is stronger than  $y$ -polarized counterpart, rather than the inversed case shown for pattern A in Fig. 4(b). In Fig. 5(c), the electric field  $E_x$  distributions are plotted for  $x$ - and  $y$ -polarized incidence with different phases at the wavelength of  $1.86\ \mu\text{m}$ . In comparison with pattern A, the extended length of Component 1 in pattern A4 causes the different field distribution and mode coupling, and hence a smaller mode amplitude under  $x$ -polarized incidence rather than that

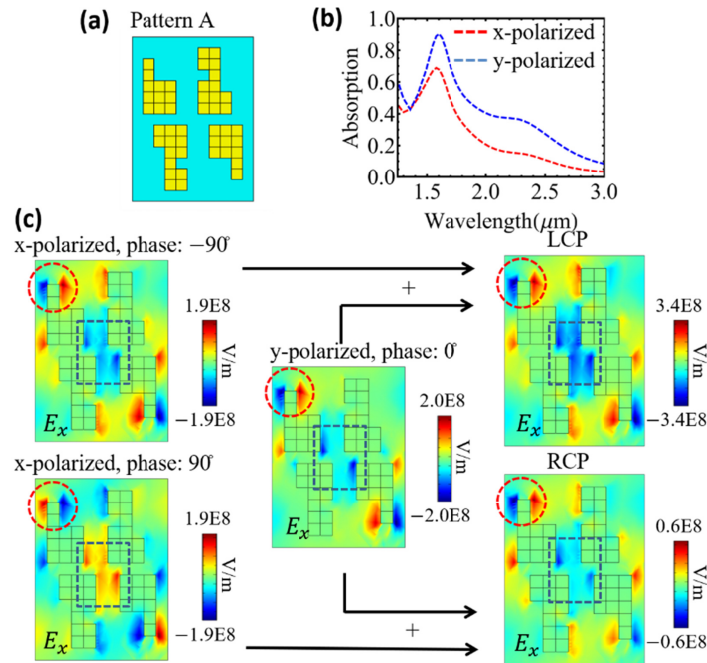


**Fig. 4.** Circular dichroic mode analysis for chiral metasurface with pattern A. (a) Schematic of the top view of chiral metasurface with pattern A. (b) Simulated absorption spectra under  $x$ - and  $y$ - polarized light at normal incidence. (c) The constructive or destructive interferences of the electric field  $E_x$  under  $x$ - and  $y$ -polarized incidence with a relative phase delay of  $90^\circ$  or  $-90^\circ$ , leading to the circular dichroic modes under LCP and RCP incidence. All modes are plotted at the surface of the top Au pattern at the resonant wavelength of  $1.62 \mu\text{m}$ .

for  $y$ -polarized incidence. Similarly, when illuminating with circularly polarized light, the LCP or RCP resonant mode is formed according to the simultaneously excited and interfered dipole modes under  $x$ - and  $y$ -polarized incidence. However, for LCP incidence, due to the adverse influence brought by the geometric parameter variation, the electric field enhancement stemmed from the constructive interference is weakened compared to that of pattern A. The obtained  $E_x$  amplitude in the LCP mode is only around 3.5 times larger than that of the RCP mode, resulting in a relatively degraded CDA. Therefore, it can be established that the chirality performance of the designed binary-pattern chiral metasurface is sensitive to the variations of critical geometric parameters.

To fully understand the wave propagation and energy absorption inside the designed chiral metasurfaces, the magnetic field distributions at certain cross sections of pattern A located at red dashed lines of a-a and b-b in the  $x$ - $z$  plane shown in Fig. 6(a) are investigated. Figure 6(b) plots the cross-sectional magnetic field  $H_y$  distribution at position a-a at the resonant wavelength of  $1.62 \mu\text{m}$ . Magnetic dipoles are observed around the metallic material but showing different mode distributions under LCP and RCP excitation. The magnetic field under LCP excitation induces stronger circulating currents represented by the black arrows between two supercell components than those for RCP excitation. Similarly, complex magnetic mode distributions and circulating currents are found at position b-b as shown in Fig. 6(c). When comparing the  $H_y$  amplitude at two cross section locations, stronger mode excitation and hence a larger contribution to the energy absorption can be found for the cross section at position a-a than those at position b-b. Furthermore, Fig. 6(d) plots the time-averaged optical power dissipation density  $Q_h$  distributions

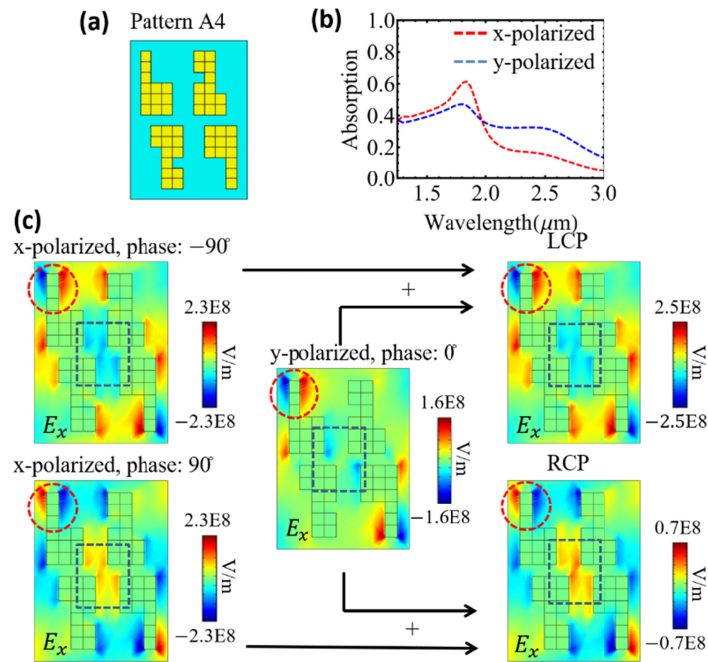


**Fig. 5.** Circular dichroic mode analysis for chiral metasurface with pattern A4. (a) Schematic of the top view of chiral metasurface with pattern A4. (b) Simulated absorption spectra under *x*- and *y*- polarized incidence at normal direction. (c) The constructive or destructive interferences of the electric field  $E_x$  under *x*- and *y*-polarized incidence with a relative phase delay of  $90^\circ$  or  $-90^\circ$ , leading to the circular dichroic modes under LCP and RCP incidence. All modes are plotted at the surface of the top Au pattern at the resonant wavelength of  $1.86 \mu\text{m}$ .

under LCP or RCP incidence located at position a-a at the resonant wavelength of  $1.62 \mu\text{m}$ .  $Q_h$  is calculated with the formula [35],  $Q_h = \epsilon_0 \omega \epsilon_m''(\omega) |E|^2 / 2$ , where  $\epsilon_0$  and  $\epsilon_m''$  denote the permittivity in vacuum and the imaginary part of the permittivity of metal. The circularly polarized light flows into the nanostructure in the way depicted through the direction and magnitude of the Poynting vector (green arrows). Compared to RCP excitation, the stronger circular dichroic mode interactions under LCP excitation leads to higher energy dissipation density. Similar energy dissipation phenomena are also observed in Fig. 6(e) at position b-b, however, the maximum dissipation density value under either LCP or RCP excitation is lower compared with that at position a-a.

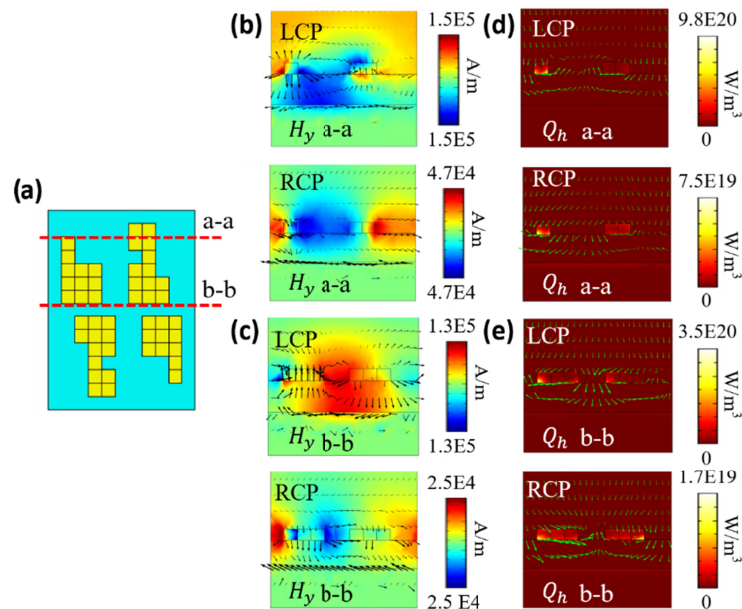


**Fig. 6.** (a) Schematic of cross sections at positions a-a and b-b. (b), (c) Cross-sectional magnetic field  $H_y$  distributions under LCP or RCP incidence located at position a-a and position b-b in the  $x$ - $z$  plane, respectively. The black arrows represent the direction and magnitude of the induced current density due to the magnetic field. (d), (e) Cross-sectional time-averaged optical power dissipation density  $Q_h$  distributions under LCP or RCP incidence located at position a-a and position b-b, respectively. Green arrows describe the direction and magnitude of Poynting vector. All fields are plotted at the resonant wavelength of 1.62  $\mu\text{m}$ .

## 6. Conclusion

Binary-pattern chiral plasmonic metasurfaces have been designed to realize strong circular dichroism in absorption at near-infrared wavelength range by using the micro-genetic algorithm optimization method. Two types of chiral metasurfaces are demonstrated through the optimization method with the measured CDA values of 0.63 and 0.60, respectively. It is shown that the chirality of the designed metasurfaces remains robust when the gap space between the supercell components is varied, but the chirality is sensitive to the variations in length and width of the components even at single pixel modification. The obtained strong CDA is explained as the results of constructive and destructive field interferences of resonance modes with relative phase delay under orthogonal linear polarizations. The absorption of the incident light is further discussed with the energy dissipation density distributions. This work provides an effective method to realize the on-demand design of chiral nanostructures with high performance, with promising great impact on applications involving chemical and biological chiral sensing, chiral imaging and spectroscopy, and nonlinear optics.

## Funding

National Science Foundation (DMR-1552871, ECCS-1653032); Office of Naval Research (N00014-16-1-2408); U.S. Department of Energy (DE-AC02-06CH11357).

## Acknowledgments

This work was performed, in part, at the Center for Nanoscale Materials, a U.S. Department of Energy Office of Science User Facility, and supported by the U.S. Department of Energy, Office of Science, under Contract No. DE-AC02-06CH11357. The authors acknowledge the support from the Intelligent Systems Center and the facility support from the Materials Research Center at Missouri S&T.

## References

1. V. A. Fedotov, P. L. Mladyonov, S. L. Prosvirnin, A. V. Rogacheva, Y. Chen, and N. I. Zheludev, "Asymmetric propagation of electromagnetic waves through a planar chiral structure," *Phys. Rev. Lett.* **97**(16), 167401 (2006).
2. W. Li, Z. J. Coppens, L. Vázquez, W. Wang, A. O. Govorov, and J. Valentine, "Circularly polarized light detection with hot electrons in chiral plasmonic metamaterials," *Nat. Commun.* **6**(1), 8379 (2015).
3. L. Kang, S. Lan, Y. Cui, S. P. Rodrigues, Y. Liu, D. H. Werner, and W. Cai, "An Active Metamaterial Platform for Chiral Responsive Optoelectronics," *Adv. Mater.* **27**(29), 4377–4383 (2015).
4. J. Hu, X. Zhao, Y. Lin, A. Zhu, X. Zhu, P. Guo, B. Cao, and C. Wang, "All-dielectric metasurface circular dichroism waveplate," *Sci. Rep.* **7**(1), 41893 (2017).
5. N. Liu and H. Giessen, "Three-dimensional optical metamaterials as model systems for longitudinal and transverse magnetic coupling," *Opt. Express* **16**(26), 21233–21238 (2008).
6. Y. Cui, L. Kang, S. Lan, S. Rodrigues, and W. Cai, "Giant chiral optical response from a twisted-arc metamaterial," *Nano Lett.* **14**(2), 1021–1025 (2014).
7. Y. Zhao, A. N. Askarpour, L. Sun, J. Shi, X. Li, and A. Alù, "Chirality detection of enantiomers using twisted optical metamaterials," *Nat. Commun.* **8**(1), 14180 (2017).
8. J.-G. Yun, J. Sung, S.-J. Kim, and B. Lee, "Simultaneous control of polarization and amplitude over broad bandwidth using multi-layered anisotropic metasurfaces," *Opt. Express* **26**(23), 29826–29836 (2018).
9. J. Sperrhake, M. Decker, M. Falkner, S. Fasold, T. Kaiser, I. Staude, and T. Pertsch, "Analyzing the polarization response of a chiral metasurface stack by semi-analytic modeling," *Opt. Express* **27**(2), 1236–1248 (2019).
10. J. K. Gansel, M. Thiel, M. S. Rill, M. Decker, K. Bade, V. Saile, G. Von Freymann, S. Linden, and M. Wegener, "Gold helix photonic metamaterial as broadband circular polarizer," *Science* **325**(5947), 1513–1515 (2009).
11. M. Esposito, V. Tasco, F. Todisco, M. Cusunà, A. Benedetti, D. Sanvitto, and A. Passaseo, "Triple-helical nanowires by tomographic rotatory growth for chiral photonics," *Nat. Commun.* **6**(1), 6484 (2015).
12. E. Plum, X. X. Liu, V. A. Fedotov, Y. Chen, D. P. Tsai, and N. I. Zheludev, "Metamaterials: Optical activity without chirality," *Phys. Rev. Lett.* **102**(11), 113902 (2009).
13. E. Plum, V. A. Fedotov, and N. I. Zheludev, "Specular optical activity of achiral metasurfaces," *Appl. Phys. Lett.* **108**(14), 141905 (2016).
14. Y. Chen, J. Gao, and X. Yang, "Direction-Controlled Bifunctional Metasurface Polarizers," *Laser Photonics Rev.* **12**(12), 1800198 (2018).
15. A. Hoorfar, "Evolutionary programming in electromagnetic optimization: A review," *IEEE Trans. Antennas Propag.* **55**(3), 523–537 (2007).
16. J. A. Bossard, L. Lin, S. Yun, L. Liu, D. H. Werner, and T. S. Mayer, "Near-ideal optical metamaterial absorbers with super-octave bandwidth," *ACS Nano* **8**(2), 1517–1524 (2014).
17. S. Jafar-Zanjani, S. Inampudi, and H. Mosallaei, "Adaptive Genetic Algorithm for Optical Metasurfaces Design," *Sci. Rep.* **8**(1), 11040 (2018).
18. C. Y. Kao, S. Osher, and E. Yablonovitch, "Maximizing band gaps in two-dimensional photonic crystals by using level set methods," *Appl. Phys. B: Lasers Opt.* **81**(2–3), 235–244 (2005).
19. B. Vial and Y. Hao, "Topology optimized all-dielectric cloak: design, performances and modal picture of the invisibility effect," *Opt. Express* **23**(18), 23551–23560 (2015).
20. S. K. Goudos and J. N. Sahalos, "Microwave absorber optimal design using multi-objective particle swarm optimization," *Microw. Opt. Technol. Lett.* **48**(8), 1553–1558 (2006).
21. S. Roy, S. D. Roy, J. Tewary, A. Mahanti, and G. K. Mahanti, "Particle Swarm optimization for optimal design of broadband multilayer microwave absorber for wide angle of incidence," *Prog. Electromagn. Res. B* **62**, 121–135 (2015).
22. W. Ma, F. Cheng, and Y. Liu, "Deep-Learning-Enabled On-Demand Design of Chiral Metamaterials," *ACS Nano* **12**(6), 6326–6334 (2018).
23. D. Liu, Y. Tan, E. Khoram, and Z. Yu, "Training Deep Neural Networks for the Inverse Design of Nanophotonic Structures," *ACS Photonics* **5**(4), 1365–1369 (2018).
24. J. Jiang, D. Sell, S. Hoyer, J. Hickey, J. Yang, and J. A. Fan, "Free-Form Diffractive Metagrating Design Based on Generative Adversarial Networks," *ACS Nano* **13**(8), 8872–8878 (2019).
25. I. Sajedian, J. Kim, and J. Rho, "Finding the optical properties of plasmonic structures by image processing using a combination of convolutional neural networks and recurrent neural networks," *Microsyst. Nanoeng.* **5**(1), 27 (2019).
26. J. A. Bossard, S. Yun, D. H. Werner, and T. S. Mayer, "Synthesizing low loss negative index metamaterial stacks for the mid-infrared using genetic algorithms," *Opt. Express* **17**(17), 14771–14779 (2009).

27. Z. Li, L. Stan, D. A. Czaplewski, X. Yang, and J. Gao, "Broadband infrared binary-pattern metasurface absorbers with micro-genetic algorithm optimization," *Opt. Lett.* **44**(1), 114–117 (2019).
28. C. Akturk, M. Karaaslan, E. Ozdemir, V. Ozkaner, F. Dincer, M. Bakir, and Z. Ozer, "Chiral metamaterial design using optimized pixelated inclusions with genetic algorithm," *Opt. Eng.* **54**(3), 035106 (2015).
29. D.-H. Kwon, P. L. Werner, and D. H. Werner, "Optical planar chiral metamaterial designs for strong circular dichroism and polarization rotation," *Opt. Express* **16**(16), 11802–11807 (2008).
30. Q. Hong, T. X. Wu, X. Zhu, R. Lu, and S.-T. Wu, "Designs of wide-view and broadband circular polarizers," *Opt. Express* **13**(20), 8318–8331 (2005).
31. S. Chakravarty, R. Mitra, and N. R. Williams, "Application of a microgenetic algorithm (MGA) to the design of broad-band microwave absorbers using multiple frequency selective surface screens buried in dielectrics," *IEEE Trans. Antennas Propag.* **50**(3), 284–296 (2002).
32. T. L. Pu, K. M. Huang, B. Wang, and Y. Yang, "Application of micro-genetic algorithm to the design of matched high gain patch antenna with zero-refractive-index metamaterial lens," *J. Electromagn. Waves Appl.* **24**(8–9), 1207–1217 (2010).
33. R. L. Olmon, B. Slovick, T. W. Johnson, D. Shelton, S. H. Oh, G. D. Boreman, and M. B. Raschke, "Optical dielectric function of gold," *Phys. Rev. B* **86**(23), 235147 (2012).
34. I. H. Malitson, "Interspecimen Comparison of the Refractive Index of Fused Silica," *J. Opt. Soc. Am.* **55**(10), 1205 (1965).
35. J. Hao, L. Zhou, and M. Qiu, "Nearly total absorption of light and heat generation by plasmonic metamaterials," *Phys. Rev. B* **83**(16), 165107 (2011).